An Adaptive Digital Stain Separation Method for Deep Learning-based Automatic Cell Profile Counts

Palak Dave[a,*], Saeed Alahmari[a], Dmitry Goldgof[a], Lawrence O. Hall[a], Hunter Morera[a], Peter R. Mouton[a,b]

[a]*Department of Computer Science and Engineering, University of South Florida, Tampa, Florida, 33620, USA*
[b]*SRC Biosciences, Tampa, Florida 33606, USA*

Abstract

Background. Quantifying cells in a defined region of biological tissue is critical for many clinical and preclinical studies, especially in the fields of pathology, toxicology, cancer and behavior. As part of a program to develop accurate, precise and more efficient automatic approaches for quantifying morphometric changes in biological tissue, we have shown that both deep learning-based and hand-crafted algorithms can estimate the total number of histologically stained cells at their maximal profile of focus in extended depth of field (EDF) images. Deep learning-based approaches show accuracy comparable to manual counts on EDF images but significant enhancement in reproducibility, throughput efficiency and reduced error from human factors. However, a majority of the automated counts are designed for *single-immunostained* tissue sections.

New Method. To expand the automatic counting methods to more complex dual-staining protocols, we developed an adaptive method to separate stain color channels on images from tissue sections stained by a primary immunostain with secondary counterstain.

Comparison with Existing Methods. The proposed method overcomes the limitations of the state-of-the-art stain-separation methods, like the requirement

*Corresponding author
Email address: palakdave@usf.edu (Palak Dave)

of pure stain color basis as a prerequisite or stain color basis learning on each image.

Results. Experimental results are presented for automatic counts using deep learning-based and hand-crafted algorithms for sections immunostained for neurons (Neu-N) or microglial cells (Iba-1) with cresyl violet counterstain.

Conclusion. Our findings show more accurate counts by deep learning methods compared to the handcrafted method. Thus, stain-separated images can function as input for automatic deep learning-based quantification methods designed for single-stained tissue sections.

Keywords: Microscopy Images, Digital Stain Separation, Automatic Cell Profile Counting, Extended Depth of Field (EDF) images, Deep Learning

1. Introduction

Automatic deep neural network-based methods have the potential to accelerate research through accurate, reproducible and efficient analyses of stained tissue sections. As part of our effort to combine deep learning (DL) and unbiased stereology methods, we have shown that digital frameworks involving extended depth of field (EDF) images created from 3D tissue volumes ("disector stacks") can be combined with hand-crafted and machine learning algorithms to enable automated and semi-automated counts with high levels of accuracy, precision and efficiency compared to manual counting methods. (All of the cells in a stack are in focus in an EDF image. EDF images are described in detail in subsection 3.2.1. "Disector stacks" are z-axis image stacks from one x-y location in tissue sections containing the anatomically defined region of interest (reference volume). The term "disector" refers to the 3D virtual probe used for thin-focal plane optical scanning in the z-axis for stereology-based cell counting, e.g., physical disector ([1]), optical disector ([2]), optical fractionator ([3]); for detailed reviews of unbiased stereology, see [4, 5].) A majority of the automatic

cell counting in 'disector stacks' approaches are designed for single immunostained tissue sections ([6]; [7]; [8]; [9]). However, many histology protocols use multiple histochemical stains, e.g., hematoxylin and eosin (H&E), combinations of a diaminobenzidine (DAB)-based immunostain and a histochemical counterstain. Stain separation can capacitate any of the available methods designed for single immunostained cells to quantify distinct cell populations stained by multiple dyes and techniques on the same tissue sections. Stain separation is often performed as one of the initial steps in the automatic cell counting methods designed for multi-stained images as well ([10, 11, 12]) to remove the extra information from the multi-stained images thereby allowing the cell quantifying methods to better focus on the objects of interest.

Alahmari et al. [7] presented an automatic counting framework for EDF images from single-immunostained tissue sections using a combination of the hand-crafted Adaptive Segmentation Algorithm (ASA) and a Deep Learned model (DL), hereafter ASA-DL. The present work extends the ASA-DL framework to color images with dual staining, e.g., NeuN for neurons with cresyl violet (CV) staining for Nissl substance. The motivation behind this work is three-fold. First, the hand-crafted ASA method was designed for gray-scale images of single-immunostained tissue sections. The ASA-DL framework uses this ASA approach to automatically generate ground truth masks on gray-scale images for training a convolutional neural network (CNN) to make automatic counts on EDF images. The advantage of the ASA step is a massive reduction in the effort required by an expert to manually generate ground truth masks by outlining boundaries in the training data. The second purpose of this work is to convert the color images of the counterstained tissue sections to gray-scale images to serve as input images to the deep learned (DL) model of the ASA-DL framework. Though a new DL model can be designed to process the color images instead of gray-scale images, this approach would require a substantial training data because of the high amount of information carried by the color images; and, training data is typically limited in many biomedical applications. Furthermore, stain color variation within and between laboratories is inevitable. A study by

Tellez et al. [13] on Whole Slide Images (WSI) regarding effects of stain color normalization on CNNs found that converting the color images to grayscale is the best performing method of stain color normalization among classical methods; that is, the color-to-gray conversion suppresses the effect of stain color variation on CNNs. As, a deep learning model trained with color information would not be generic for different stain types, we propose a digital stain separation approach using an adaptive method for color-to-gray transformation. Here we show that our ASA-DL framework achieves superior results to ASA alone, that isolation of the immunostain channel from immunostained/counterstained color images gives comparable counts to immunostained color images and that this approach works for different immunostains and multiple cell types (neurons, microglia cells). Though this study focuses on automatic counts of cells at their maximal plane of focus in synthetic EDF images created from 3-D volumes of digital images, i.e., disector stacks, the second phase of this work (to be published separately) uses the same color separation approach in combination with slice-wise analysis of each image in the disector stack to make automatic estimates of the total number of immunostained cells using the unbiased optical fractionator method [3].

In the ASA-DL framework, the color images of single-stain tissue sections were converted to grayscale using the conventional BT.601-7 (studio encoding parameters for digital television) Equation 1, [14]. In Equation 1, R, G, and B are the intensity values of the red, green, and blue channels respectively. Y is the gray scale intensity value. If the color images of counter-stained tissue sections are converted to grayscale using the conventional BT.601-7 transformation or an advanced method like correlation based color to gray conversion proposed by [15], both stains become so similar in appearance it becomes difficult for a human observer to discriminate between them. Figure 1 shows an example of such conversions. This approach entails a pre-processing step to first digitally separate the information about two stains present in one image into two separate

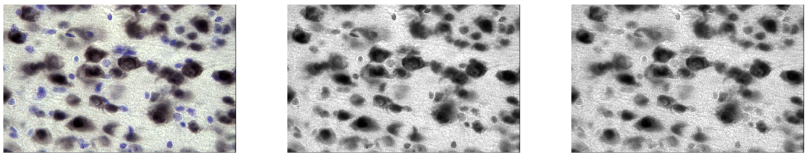

(a) Color image of counter-stained tissue section (NeuN-DAB&CV)

(b) Gray scale image converted using BT.601-7, [14]

(c) Gray scale image converted using CorrC2G method, [15]

Figure 1: Example of color to gray conversion using existing methods.

images. This process is referred as stain separation.

$$Y = 0.2989 * R + 0.5870 * G + 0.1140 * B \tag{1}$$

2. Related Work

Stain color normalization is a process of digitally standardizing image appearance in histology, [16]. [17] presented a detailed study of stain color normalization methods published in the past two decades. These methods use two major approaches: 1. Global color normalization like histogram specification; and, 2. Color normalization after stain separation by supervised or unsupervised methods. The goal of stain separation is to obtain a separate image called a stain density map corresponding to each stain in the input image. The intensity at each pixel of a stain density map represents an estimated amount of the corresponding stain present at that location. The qualitative and quantitative results of the study published in [17] find the Structure-Preserving Color Normalization (SPCN) method presented by [16] to be the best performing method. The major advantage of using this method is that it incorporates stain mixing. The work in our present approach uses the principal stain density map as a gray-scale image input to the ASA-DL framework for automatic counts of cell profiles from dual-stained tissue sections.

The majority of the stain color normalization methods [[18]; [19]; [20]], including SPCN ([16]), use Equation 2 derived from Equations 3 and 4 for stain

separation. Equation 3 represents the Beer-Lambert law as a non-linear relationship between a pixel intensity and stain density. Due to the non-linear relationship between image intensity and the stain density, it is inconvenient to work in the image intensity space to estimate the stain density maps. If $m \times n$ is the image dimension, let I of dimensions $3 \times mn$ be the RGB pixel intensities normalized in the range of [0,1] and r be the number of stains. C is the stain color basis ($3 \times r$), where each column is essentially a wavelength specific (R,G and B) absorptivity coefficient vector of a stain. D is the stain density map with dimensions $r \times mn$. Optical density, O ($3 \times mn$), is defined as the logarithm of normalized intensity as shown in Equation 4. Equation 2 shows a linear relationship between Optical density (O) and stain density (D). Hence, it is convenient to work in the O space, instead of intensity space, to estimate the D maps. The stain color normalization methods mentioned earlier [[18]; [19]; [20]; [16]] work in the O space.

$$O \propto CD \tag{2}$$

$$I = e^{-CD} \tag{3}$$

$$O = -\log_{10} I \tag{4}$$

A widely used method for stain separation is called *color deconvolution* ([18]). O is an observation available from an image and a fixed deconvolution matrix or stain color basis (C) is computed from control images of tissue sections with one pure stain at a time. D is estimated using Equation 2. However, variations in stain appearance are highly frequent in histology due to protocol variations from stain concentration and duration of staining. Also, while the biological structures like nuclei or cytoplasm bind tightly with either the principal or counter stain, they also absorb some amount of the other stain ([16]). As a result, stain color basis computed using pure stain images would not be accurate. Moreover, chemical staining-destaining of a tissue section to get control images may not be feasible or practical for every new stain.

An unsupervised stain separation method using Non-negative Matrix Factorization (NMF) was proposed by [19] to learn an image specific stain color basis. A non-negative constraint was imposed on C and D based on the fact that stain color basis and stain density cannot be negative. However, this method may get to a local optimum solution because it attempts a joint non-convex optimization (Equation 5) ([16]).

$$\begin{aligned} \min_{C,D} \quad & \frac{1}{2}||O - CD||^2 \\ \text{s.t.} \quad & C, D >= 0 \end{aligned} \tag{5}$$

[16] presented a Sparse Non-negative Matrix Factorization (SNMF) method for unsupervised stain separation. This method added a sparsity constraint in the objective function of the NMF method and alternately optimized only one of the two variables C and D at a time by keeping the other fixed. We use this method with a few modifications (different value of a hyper-parameter and using a fixed stain color basis as described in section 3) for this work.

[21] proposed a digital stain separation method in RGB and HSV color space instead of O space. However, this method requires customization for type of stain and number of stains. The method proposed here is generic for any stain type and the number of stains is a parameter (r) to be supplied.

It should be noted that DAB stain is not a true absorber of light but rather scatters light and hence, does not follow the Beer-Lambert law [22]. This means that the relationship between stain density (D) and its Optical Density (O) is non-linear. This suggests that O of DAB is not suitable to accurately quantify the stain intensity. However, as mentioned by [22], DAB can be successfully unmixed from a counterstained stain image. This means, it can be used for counting applications, but not for applications that rely on accurate quantification of the stain.

3. Methods

An overview of the complete automatic counting system with an example of a microglia image stack is presented in Figure 2. The details are discussed in the following subsections.

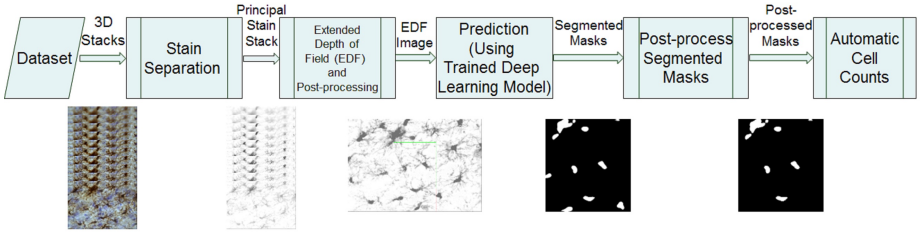

Figure 2: An overview of the automatic counting system

3.1. Color to Gray Conversion using Stain Separation

The proposed stain separation method based on SNMF for color to gray conversion and its application on 3D stacks is discussed in this section.

3.1.1. Stain Separation using SNMF

As mentioned in the previous section, we used SNMF with a few modifications for the stain separation. [16] proposed a Sparse Non-negative Matrix Factorization (SNMF) formulation (Equation 6) by adding an l_1 sparsity constraint in the NMF formulation and solved the non-convex optimization problem by alternately optimizing over one variable while keeping the other constant, [16]. The sparsity constraint is to incorporate stain mixing and was derived from the fact that each biological structure (like nuclei or cytoplasm) can bind to both the stains (principal and counter stain) and not only to a pure stain. Selection of SNMF for stain separation in this work is also supported by the qualitative and quantitative comparison results of the study performed by [17].

In Equation 6, Optical Density (O) reflects the observations available from an image, and C and D are estimated by learning. The additional constraint

on C to have unit Euclidean norm for each color basis is to suppress multiple equivalent solutions of type $(C/\alpha, \alpha D)$, $\alpha > 0$.

$$\begin{aligned} \min_{C,D} \quad & \frac{1}{2}||O - CD||^2 + \lambda \sum_{i=1}^{r} ||D(i,:)||_1 \\ \text{s.t.} \quad & C, D >= 0, \\ & ||C(:,i)||_2^2 = 1 \end{aligned} \tag{6}$$

SNMF has λ as a sparsity and regularization coefficient. This hyper-parameter controls the amount of stain mixing incorporated during stain separation. [16] recommended to use $\lambda = 0.1$ based on sensitivity analysis of λ on Hematoxylin and Eosin (H&E) stains. During stain separation, it is desirable to preserve the small amount of stain present in the background for image color normalization kinds of application, where an accurate quantification of the stains on the complete image is required. On the contrary, presence of a small amount of stain in the background is noise for other microscopy applications like cell counting. In order to reduce this noise to a negligible level, a higher value of the sparsity coefficient can be helpful. Usually, such hyperparameter value selection is goal dependent and it is good to select a value based on cross-validation. However, such cross-validation would require many expensive training steps in the target application. In order to avoid that, we visually analyzed the contrast between foreground and background in separated stain images using different values of λ. The observed contrast was high and sufficient when $\lambda = 0.8$, getting high sparsity in the solution. Figure 3 shows DAB stain density maps computed with $\lambda = 0.1$ and $\lambda = 0.8$.

3.1.2. Color to Gray Conversion

The result of stain separation provides separate stain density maps corresponding to each stain (DAB & CV). The DAB - principal stain density map was used as gray-scale image input to the ASA-DL framework for automatic counting ([7]). A fixed transformation is applied to map an admissible continuous range of the stain density values to a discrete range of [0,255]. Figures 4b

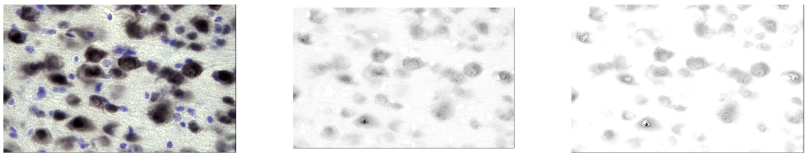

(a) Color image of a counterstained tissue section (DAB & CV stains)

(b) DAB stain density map using $\lambda = 0.1$

(c) DAB stain density map using $\lambda = 0.8$

Figure 3: Stain separation result using SNMF method with different values of λ.

and 4c show density maps as gray-scale images after stain separation.

3.2. Processing 3D Stacks

A method of representing 3D information distributed among a stack of images in a 2D image and a post-processing step to visually match such 2D images of the counterstain dataset to that of the single stain dataset is discussed in this section.

3.2.1. 3D to 2D Conversion

The optical fractionator is commonly used in stereology to estimate the number of cells in a 3-D optical disector volume, consisting here of a stack of n images (ten 1 µm images), by thin focal-plane optical scanning along the z-axis then repeating in a known fraction of a defined reference volume [3]. This is explained in more detail in Section 3.4. Individual cells occur in optimal focus in different images of a disector stack based on their physical location in the tissue. Here all the images of a stack are first converted to stain density maps. As the cell nuclei tightly bind to the principal stain (DAB), processing only the DAB stain density maps is required for automatic counting. The 3D information distributed among the DAB density-map stack is represented in a 2D image by converting it to an Extended Depth of Field (EDF) image using an over-complete discrete wavelet transform based algorithm proposed by [23]. All of the cells in a stack are in focus in an EDF image. When working with EDF images there is an over-projection issue that varies according to the degree of

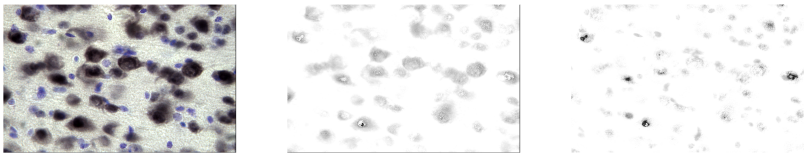

(a) Color image of a counter-stained tissue section (DAB & CV stains)

(b) DAB stain density map

(c) CV stain density map

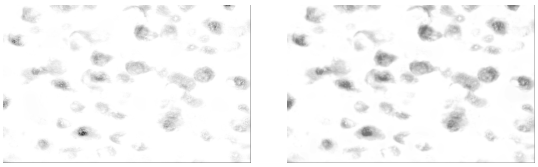

(d) EDF, before post-processing, of stack corresponding to 4b

(e) EDF, after post-processing, of stack corresponding to 4b

Figure 4: Stain density maps after stain separation using SNMF with $\lambda = 0.8$, EDF of principal stain density maps before and after post-processing

overlap. We have used EDF images for our proof of concept studies such as the present work, since human observers also cannot see fully obscured objects. Our previous work with EDF images using hand-crafted automatic algorithms ([6]) and deep learning automatic algorithms ([7]) confirmed these approaches achieve similar accuracy to human observers; however, applications of this approach to EDF images can lead to under-counts in the case of overlapping cells. A future extension of the present approach to slice-by-slice cell counting in each disector stack will ensure accurate counts in all scenarios (overlap versus non-overlap) similar to thin focal-plane scanning with optical disectors.

3.2.2. Visually Matching Counterstain Images to Single-stain Images

To reuse the ASA-DL framework, designed and developed for the single-immunostained neuron images as presented by [7], a post-processing step is performed on the EDF image of DAB stain density maps (Figure 4d) to visually match it with that of a single-immunostained neuron image dataset. The major difference between single-immunostained EDF and DAB-EDF image of

the counterstain dataset is that the pixel intensity within cells is homogeneous and darker in single stain. In DAB-EDF, there is a large change in intensity (a very dark spot) within the cell due to high stain density in that part of the cell. To get rid of such dark spots and make the within cell intensity homogeneous, all foreground (< 255) intensities below 150 are truncated to 150. The cut-off threshold for truncation can be automatically computed by comparing the statistics of the histograms of EDFs from counterstained and single immunostained neuron datasets. The value of 150 was chosen by visual comparison of the EDFs for both datasets in this study as a proof-of-concept. This step is followed by Gaussian smoothing with standard deviation of 2. The smoothing is performed to overcome the zero stain density of some pixels within a cell. Such zero stain density pixels within a cell occur due to a high sparsity coefficient value (which helps in reducing background noise) in SNMF. The smoothing can potentially increase the size of the cells by a few pixels. However, such a change in cell size by a few pixels is not significant because, in consistency with the ASA-DL method, the minimum size of a cell is expected to be at least 250 pixels in the post-processing step depicted in Figure 5d. The smoothed image is then gamma-corrected with gamma = 1.5 to improve the image's overall darkness. Figures 4d and 4e show an example of an EDF and post-processed EDF of the stack corresponding to the sample image shown in Figure 4b.

3.3. Fixing Stain Color Basis

During stain separation, a minima of the objective function (Equation 6) of SNMF is estimated by applying unsupervised learning on each image. The objective is to minimize the cost over the complete image. However, in some images, the two stains are present in largely imbalanced proportion. In such images, two different shades of a dominant stain are learnt as two different stains, leading to erroneous stain separation. To eliminate this problem, a fixed stain color basis is used for a given stain. The fixed stain color basis is computed using a subset of the dataset. From the five mice in the NeuN counterstain dataset (described in Section 3.4), we randomly selected three mice, two sections per

mouse, one stack per section, and two images per stack. SNMF based stain separation was performed on each image of this subset of twelve images under manual observation. A human observer can accept or reject the results of stain separation on each of the twelve images. This requires less than 30 minutes of human observer time. The stain color bases of accepted images are averaged, and this average value is used as a fixed stain color basis for stain separation on complete NeuN counterstain and IBA1 counterstain datasets (described in Section 3.4). It is noteworthy that averaging of the accepted stain color bases can potentially violate the unit Euclidean norm constraint on columns of C in Equation 6. Practically, the values of the accepted stain color bases are very close and hence, the constraint violation is minor. Further, this violation would not be fundamentally problematic for stain separation in the target application since the constraint was used just to suppress multiple equivalent solutions. This fixed stain color basis shows satisfactory results on the images from mice not present in the learning subset and on a dataset of a different cell type (Microglia-IBA1) with the same stains. Moreover, the fixed stain color basis speeds up the stain separation process as well by eliminating the stain basis learning step on each image.

3.4. Dataset

The staining protocols for dual stains are one immunostain (NeuN or Iba-1) each with cresyl violet counterstain, i.e., NeuN/CV, Iba-1/CV. Staining protocols were conventional immunostaining with primary and secondary antibodies and DAB-based colorization followed by standard counterstaining in a 2% cresyl violet (CV) solution, as we have previously detailed ([24]). We collected Z-axis stacks of images (disector stacks) using the Stereologer system consisting of an Olympus microscope equipped with automatic stepping motors. Disector stacks were acquired using systematic-random sampling, starting at a random X-Y location in the upper left quadrant of neocortex in the first section, proceeding in a systematic manner at intervals of 1200 µm × 1200 µm, and repeating on 8-12 sections through the entire mouse neocortex. This sampling approach provides

for low sampling error as evidenced by coefficient of error (CE) $\sim$ 0.10 (CE $\sim$ 10%), as shown by [25]. The number of animals for this study was five for the NeuN and eight for the IBA1 dataset.

As mentioned above, the images for this study were collected using the following sampling hierarchy. First, a total of about 8 to 12 tissue sections were collected by systematic-random sampling through the entire neocortex of the mouse brain. Second, a total of about 10 to 12 disector probe locations (referred to as 'stacks') were collected in a systematic-random manner from each section. Finally, at each disector probe location, a series of 10 images at different focal planes along the z-axis were captured at each disector probe location. In other words, a systematic-random sample of z-axis images (disector stacks) representing a known fraction of the reference space was created, i.e., similar to the disector volumes analyzed by the ordinary optical fractionator method used to make total number estimates for cells in an anatomically defined reference space. Gundersen's unbiased counting rules ([26]) were applied to avoid edge effects when counting in a 3D stack of z-axis images (i.e., disector stack) as shown in Figures 6(c) and 6(f). That is, profiles were included that fell within the disector volume or touched one of the top, upper or right-side inclusion planes in 3D. Profiles were excluded that fell outside the disector volume or touched either the bottom, lower or left-side exclusion planes.

The sum of profiles counted in all disector stacks sampled in a systematic-random manner through the reference space is referred as the "Ground Truth (GT) count" in this work. The Ground Truth count was obtained manually using disector videos. As part of the development of our automatic optical fractionator, we have improved the efficiency of collecting GT counts by converting disector stacks into optical disector videos. For these manual GT counts, the user counts (clicks) on cells of interest while the disector video moves at a user-controlled variable speed through the z-stack of disector planes. In our experience, this substantially reduces the number of keyboard clicks per brain, leading to higher efficiency, as well as less tedium and fatigue for GT counts, without a loss of accuracy and precision (reproducibility) as compared to counts

by conventional manual focusing through the same disector stacks.

It is noteworthy that our work involves two levels of ground truth (GT). The first is the cell count GT that requires a click on each cell. This cell count GT is performed at the individual focal planes using videos as described above. The second GT is mask with each counted cell profile outlined; these masks are then used for training the deep learning model; these GT masks are obtained by the process explained in Figure 5a.

Two datasets with two types of brain cells, neurons (NeuN) and microglia cells (Iba-1), with the same colorization and counterstaining methods (DAB and CV, respectively) were used for the experiments presented in Section 4.1. The NeuN dataset has five mice and the IBA1 dataset has eight mice. A summary of the datasets is provided in Tables 1 and 2. Here, the column 'Number of Images' refers to the number of stacks after each stack is converted to an EDF image.

Mouse ID	Number of Images	Ground Truth Count
PI3-18	68	544
PI3-19	103	955
PI3-20	98	1009
PI3-21	97	1207
PI3-22	62	579

Table 1: Summary of neuron (NeuN) counterstain dataset

4. Experimental Results

In this section, experimental results from applying ASA-DL approach on stain separated images by the proposed method are discussed.

4.1. Experimental Results

The post-processed EDF images (as described in Section 3.2) are used as input to the ASA-DL framework shown in Figure 5.

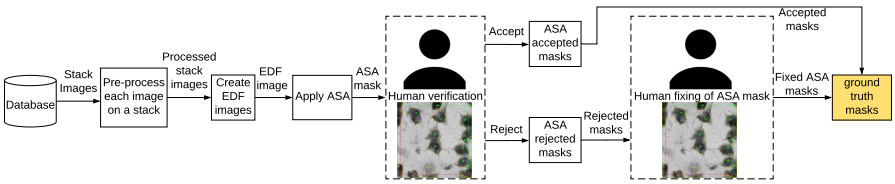

(a) Ground truth preparation

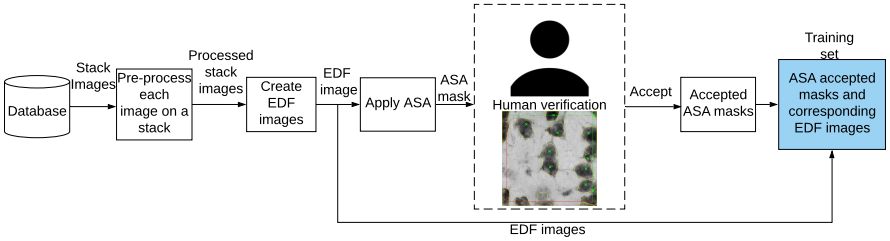

(b) Training set preparation

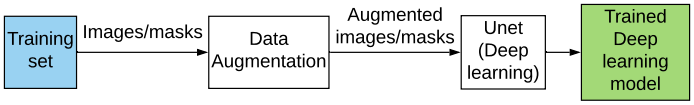

(c) Training stage

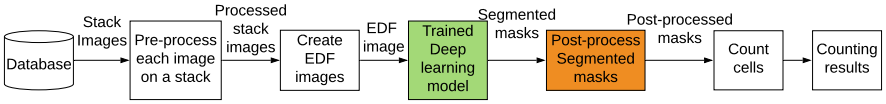

(d) Testing stage

Figure 5: The automatic counting framework (ASA-DL) proposed by [7]

Mouse ID	Number of Images	Ground Truth Count
PI3-27	129	324
PI3-28	148	392
PI3-29	143	254
PI3-31	147	166
PI3-32	105	261
PI3-33	114	271
PI3-34	147	160
PI3-35	160	172

Table 2: Summary of microglia (IBA1) counterstain dataset

Augmentation by rotation and elastic transformation was performed on training images to obtain a larger and more diverse training set to enhance the performance of the deep learning model. As discussed by [7], we used the U-Net deep learning architecture for segmentation consisting of convolution layers for encoding and then decoding to learn features and localize the learned features in the original input image for segmentation. U-Net was trained using Keras and Tensorflow frameworks for 100 epochs using the Adam optimizer and learning rate of $1e^{-4}$ ([27]; [28]; [29]). The U-Net model training occurs automatically primarily using computer time rather than time from an expert. The training time depends on the number of disector samples in the training set, hardware capacity, learning parameters etc. It takes ≈30 hours for 28080 disector samples (after augmentation) in the training set. Once the training was underway, no human observation was required. Finally, the training time is a one-time investment of resources for a particular stain type. Once the model is trained, the time to analyze new ("test") images on disector stacks is less than 30 minutes per reference space (≈100 disector stacks).

Results of automatic counting using the handcrafted algorithm ASA and using the ASA-DL approach are reported in Tables 3 and 4 for the NeuN and

Test Mouse ID	#Images	Ground Truth Count (G)	ASA Count (A)	ASA Error Rate(%) ($\frac{\lvert G-A\rvert * 100}{G}$)	ASA-DL Count (L)	ASA-DL Error Rate(%) ($\frac{\lvert G-L\rvert * 100}{G}$)
PI3-18	68	544	412	24.26	531	2.39
PI3-19	103	955	852	10.79	939	1.68
PI3-20	98	1009	817	19.03	846	16.15
PI3-21	97	1207	1014	15.99	1029	14.75
PI3-22	62	579	499	13.82	535	7.60
Average Error Rate (%)				16.78		8.51

Table 3: Automatic counting results on stain-separated NeuN counterstain dataset using ASA and ASA-DL. Where, the last column refers to % error; and, the last row refers to the Mean % error for all mice analyzed.

IBA1 dataset, respectively. The error rate is computed as a percentage of the absolute difference of automatic count with respect to ground truth count. A 5-fold cross validation experiment using a "one-subject-left-out" strategy was performed on the five mice NeuN dataset using ASA-DL approach. That is, the deep learning model was trained on image data (stacks) from four mice, with image data from one mouse left out for subsequent use as a test dataset, i.e., images not previously used for training the model. Therefore, the model's performance is validated based on unseen images not used for training the model (note- the model is expected to perform well on the images used for training the model). Since each of the five mice is left out once for testing in one of the five folds, this approach allows for cross validating the performance of the deep learning model on previously unseen images, therefore, a fair basis for validating the model's performance. A 3-fold cross validation was performed on the eight mice IBA1 dataset. Here, two of the folds had data from three mice and one fold had data from two mice left out as test set. It should be noted that the stain color basis learned using the procedure mentioned in Section 3.3, from a subset of images from the NeuN dataset, was used for both the NeuN and Iba1 datasets. Visualization of samples from both datasets is shown in Figure 6.

Test Mouse ID	#Images	Ground Truth Count (G)	ASA Count (A)	ASA Error Rate(%) ($\frac{\lvert G-A\rvert * 100}{G}$)	ASA-DL Count (L)	ASA-DL Error Rate(%) ($\frac{\lvert G-L\rvert * 100}{G}$)
PI3-27	129	324	249	23.15	356	9.88
PI3-28	148	392	299	23.72	401	2.30
PI3-29	143	254	182	28.35	241	5.12
PI3-31	147	166	129	22.29	159	4.22
PI3-32	105	261	207	20.69	273	4.60
PI3-33	114	271	209	22.88	301	11.07
PI3-34	147	160	121	24.38	145	9.38
PI3-35	160	172	148	13.95	166	3.49
Average Error Rate (%)				22.43		6.26

Table 4: Automatic counting results on stain-separated IBA1 counterstain dataset using ASA and ASA-DL. Where, the last column refers to % error; and, the last row refers to the Mean % error for all mice analyzed.

5. Discussion and Conclusion

An adaptive method is proposed to digitally separate two colors in images from dual stained tissue sections. The proposed method overcomes the limitations of the state-of-the-art methods, color deconvolution (requirement of fixed and pure stain color basis as a prerequisite) and SNMF (stain color basis learning on each image and dependency on the stain distribution in the image). A fixed stain color basis is learned on a subset of a NeuN counterstain dataset under a one-time manual observation. When applied as an automatic counting method on the stain separated images, the ASA-DL approach shows substantially higher performance than a hand-crafted automatic ASA method alone as evidenced by lower average error rates on both datasets with two different cell types.

The proposed method is an adaptive technique for color-to-gray conversion, where information related to only the object of interest, i.e., DAB-based immunostaining for neurons (NeuN) or microglial cells (Iba-1), is preserved while color related to the general counterstain (CV) is eliminated. Gray-scale images obtained through this method are used with the ASA-DL framework initially

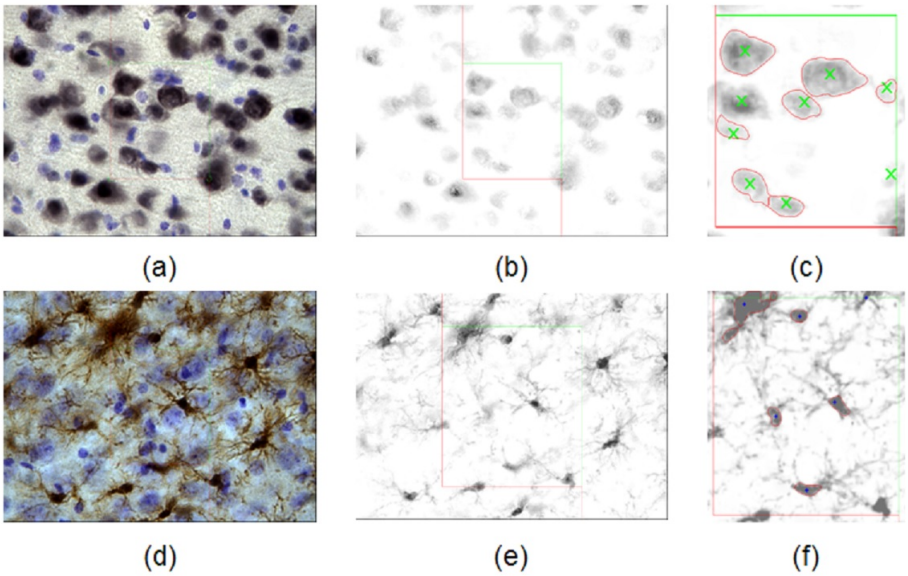

Figure 6: (a) Sample neuron (NeuN immunopositive) image with counterstain; (b) Conversion to single stain gray EDF image using proposed stain separation on (a); (c) Automatic counts of NeuN cell profiles on (b); (d) Sample microglia (Iba-1 immunopositive) image with counter stain; (e) Conversion to single stain gray image using stain separation on (d); (f) Automatic microglia counts on (e). The unbiased counting frame includes left and lower exclusion lines (red) and upper and right inclusion lines (green)(lines convert to planes in 3D). In Figures (c) and (f), the red outline around cell profiles represent automatic detection, green and blue markings are GT.

designed and developed for a single-immunostained image dataset. Initial experiments show promising results for automatic counting on five mice of the NeuN and eight mice of the Iba-1 immunostained with counterstain datasets. [7] presented automatic counting results using the ASA-DL framework for a single immunostained NeuN dataset of 9 mice. In order to compare the current results on NeuN counterstain dataset with the published result, an experiment done with a subset of 5 randomly chosen mice from the 9 mice showed an average ASA error rate of 9.42% and average ASA-DL error rate of 4.67%. The average ASA-DL error rate for the same 5 mice in the published results (when the deep learner was trained on 9 mice) is 2.67% ([7]). Following the trend of the

published results, the average error rate using ASA-DL is approximately half or less compared to that using ASA for both the counterstain datasets. Moreover, the lower error rate (2.67%) with 9 mice NeuN single immunostained dataset shows that performance for the counterstain images can be further improved by using a larger dataset.

Our proposed method is applied to dual staining with DAB-based immunostains as primary stains for neurons (NeuN) and microglial cells (Iba-1) with CV as the common counterstain. The stain separation approach is independent of these specific immunostains and counterstains. As such, it can be used as a preprocessing step in the ASA-DL framework and applied to any immunostained target object in a dual stain combination with any counterstain. Furthermore, beside automatic cell counting the proposed stain separation method is potentially applicable to other applications for automating estimation of other stereology parameters, e.g., total length estimation using the Space Balls method ([4]); total surface area using the Virtual Cycloids method ([30]). The value of the sparsity coefficient parameter can be chosen as best suited for the dataset and application.

In conclusion, this study provides a novel proof-of-concept for automatic deep learning-based counting of cell profiles in synthetic EDF images created from 3-D volumes, i.e., disector stacks. Though useful for demonstrating our stain separation method, a limitation of EDF images is the potential for undercounting due to overlapping of smaller cells by larger cells in the z-axis of disector stacks. To eliminate these undercounts, our future studies will focus on automatic counting of each cell in the disector stack using a slice-wise DL approach, thereby allowing for automatic thin focal plane scanning in the z-axis as required for unbiased stereology counts using the optical disector and optical fractionator methods. Thus, the present color separation approach will support automatic unbiased stereology counts of the total number of immunostained cells on dual-stained tissue sections.

Acknowledgments

Authors would like to thank Dr. Hady Ahmady Phoulady for his prior work in the program. Authors also thank Raj Patel for his help with the data collection for the work presented in this manuscript.

Funding. This work was supported by National Science Foundation Grant# 1926990 (SRC Biosciences), Florida High Tech Corridor Grant# 20-10 and National Science Foundation Grant# 1513126 (University of South Florida)

Declaration of Interests

The authors declare that they have no known competing financial interests or personal relationships that could have appeared to influence the work reported in this paper.

References

[1] D. Sterio, The unbiased estimation of number and sizes of arbitrary particles using the disector, Journal of microscopy 134 (2) (1984) 127–136.

[2] H.-J. G. Gundersen, Stereology of arbitrary particles* a review of unbiased number and size estimators and the presentation of some new ones, in memory of william r. thompson, Journal of microscopy 143 (1) (1986) 3–45.

[3] M. West, L. Slomianka, H. J. G. Gundersen, Unbiased stereological estimation of the total number of neurons in the subdivisions of the rat hippocampus using the optical fractionator, The Anatomical Record 231 (4) (1991) 482–497.

[4] P. R. Mouton, Principles and practices of unbiased stereology: an introduction for bioscientists, JHU Press, 2002.

[5] P. R. Mouton, Unbiased stereology: a concise guide, JHU Press, 2011.

[6] P. R. Mouton, H. A. Phoulady, D. Goldgof, L. O. Hall, M. Gordon, D. Morgan, Unbiased estimation of cell number using the automatic optical fractionator, Journal of Chemical Neuroanatomy 80 (2017) A1 – A8. doi:https://doi.org/10.1016/j.jchemneu.2016.12.002.
URL http://www.sciencedirect.com/science/article/pii/S089106181630223X

[7] S. S. Alahmari, D. Goldgof, L. Hall, H. A. Phoulady, R. H. Patel, P. R. Mouton, Automated cell counts on tissue sections by deep learning and unbiased stereology, Journal of Chemical Neuroanatomy 96 (2019) 94 – 101. doi:https://doi.org/10.1016/j.jchemneu.2018.12.010.
URL http://www.sciencedirect.com/science/article/pii/S0891061818300929

[8] S. Alahmari, D. Goldgof, L. Hall, P. Dave, H. A. Phoulady, P. Mouton, Iterative deep learning based unbiased stereology with human-in-the-loop, in: 2018 17th IEEE International Conference on Machine Learning and Applications (ICMLA), IEEE, 2018, pp. 665–670.

[9] H. A. Phoulady, D. Goldgof, L. O. Hall, P. R. Mouton, Automatic ground truth for deep learning stereology of immunostained neurons and microglia in mouse neocortex, Journal of chemical neuroanatomy 98 (2019) 1–7.

[10] T. Chen, C. Chefd'Hotel, Deep learning based automatic immune cell detection for immunohistochemistry images, in: International workshop on machine learning in medical imaging, Springer, 2014, pp. 17–24.

[11] N. Rey-Villamizar, V. Somasundar, M. Megjhani, Y. Xu, Y. Lu, R. Padmanabhan, K. Trett, W. Shain, B. Roysam, Large-scale automated image analysis for computational profiling of brain tissue surrounding implanted neuroprosthetic devices using python, Frontiers in neuroinformatics 8 (2014) 39.

[12] M. Adamiak, Astrocytes instance segmentation with machine learning (2020).

URL https://blog.softwaremill.com/astrocytes-instance-segmentation-with-machine-learning-a0acb73248ce

[13] D. Tellez, G. J. S. Litjens, P. Bándi, W. Bulten, J.-M. Bokhorst, F. Ciompi, J. van der Laak, Quantifying the effects of data augmentation and stain color normalization in convolutional neural networks for computational pathology, Medical image analysis 58 (2019) 101544.

[14] ITU, Studio encoding parameters of digital television for standard 4:3 and wide screen 16:9 aspect ratios (2011).
URL https://www.itu.int/rec/R-REC-BT.601/

[15] H. Z. Nafchi, A. Shahkolaei, R. Hedjam, M. Cheriet, Corrc2g: Color to gray conversion by correlation, IEEE Signal Processing Letters 24 (11) (2017) 1651–1655. doi:10.1109/LSP.2017.2755077.

[16] A. Vahadane, T. Peng, A. Sethi, S. Albarqouni, L. Wang, M. Baust, K. Steiger, A. M. Schlitter, I. Esposito, N. Navab, Structure-preserving color normalization and sparse stain separation for histological images, IEEE transactions on medical imaging 35 (8) (2016) 1962–1971.

[17] S. Roy, A. kumar Jain, S. Lal, J. Kini, A study about color normalization methods for histopathology images, Micron.

[18] A. C. Ruifrok, D. A. Johnston, et al., Quantification of histochemical staining by color deconvolution, Analytical and quantitative cytology and histology 23 (4) (2001) 291–299.

[19] A. Rabinovich, S. Agarwal, C. Laris, J. H. Price, S. J. Belongie, Unsupervised color decomposition of histologically stained tissue samples, in: Advances in neural information processing systems, 2004, pp. 667–674.

[20] M. Macenko, M. Niethammer, J. S. Marron, D. Borland, J. T. Woosley, X. Guan, C. Schmitt, N. E. Thomas, A method for normalizing histology slides for quantitative analysis, in: 2009 IEEE International Symposium on Biomedical Imaging: From Nano to Macro, IEEE, 2009, pp. 1107–1110.

[21] P. Tadrous, Digital stain separation for histological images, Journal of microscopy 240 (2) (2010) 164–172.

[22] C. M. van der Loos, Multiple immunoenzyme staining: Methods and visualizations for the observation with spectral imaging, Journal of Histochemistry & Cytochemistry 56 (4) (2008) 313–328, pMID: 18158282. arXiv:https://doi.org/10.1369/jhc.2007.950170, doi:10.1369/jhc.2007.950170.
URL https://doi.org/10.1369/jhc.2007.950170

[23] A. P. Bradley, P. C. Bamford, A one-pass extended depth of field algorithm based on the over-complete discrete wavelet transform.

[24] P. R. Mouton, Applications of unbiased stereology to neurodevelopmental toxicology, Developmental Neurotoxicology Research. Hoboken, NJ: Wiley (2011) 53–75.

[25] H. J. G. Gundersen, E. B. V. Jensen, K. Kiêu, J. Nielsen, The efficiency of systematic sampling in stereology—reconsidered, Journal of microscopy 193 (3) (1999) 199–211.

[26] H. J. G. Gundersen, Notes on the estimation of the numerical density of arbitrary profiles: the edge effect, Journal of microscopy 111 (2) (1977) 219–223.

[27] F. Chollet, et al., Keras (2015).

[28] M. Abadi, P. Barham, J. Chen, Z. Chen, A. Davis, J. Dean, M. Devin, S. Ghemawat, G. Irving, M. Isard, et al., Tensorflow: A system for large-scale machine learning, in: 12th {USENIX} Symposium on Operating Systems Design and Implementation ({OSDI} 16), 2016, pp. 265–283.

[29] D. P. Kingma, J. Ba, Adam: A method for stochastic optimization, arXiv preprint arXiv:1412.6980.

[30] A. Gokhale, R. Evans, J. Mackes, P. Mouton, Design-based estimation of surface area in thick tissue sections of arbitrary orientation using virtual cycloids, Journal of microscopy 216 (1) (2004) 25–31.